NUMERICAL SIMULATION OF THE EFFECT OF WAVE CHARACTERISTICS ON PTO OF POINT ABSORBER WAVE ENERGY CONVERTER

An Undergraduate Research Scholars Thesis

by

ABIGAIL ROLEN

Submitted to the LAUNCH: Undergraduate Research office at
Texas A&M University
in partial fulfillment of the requirements for the designation as an

UNDERGRADUATE RESEARCH SCHOLAR

Approved by
Faculty Research Advisor: Mirjam Fürth

May 2022

Major: Aerospace Engineering

RESEARCH COMPLIANCE CERTIFICATION

Research activities involving the use of human subjects, vertebrate animals, and/or biohazards must be reviewed and approved by the appropriate Texas A&M University regulatory research committee (i.e., IRB, IACUC, IBC) before the activity can commence. This requirement applies to activities conducted at Texas A&M and to activities conducted at non-Texas A&M facilities or institutions. In both cases, students are responsible for working with the relevant Texas A&M research compliance program to ensure and document that all Texas A&M compliance obligations are met before the study begins.

I, Abigail Rolen, certify that all research compliance requirements related to this Undergraduate Research Scholars thesis have been addressed with my Research Faculty Advisor prior to the collection of any data used in this final thesis submission.

This project did not require approval from the Texas A&M University Research Compliance & Biosafety office.

TABLE OF CONTENTS

ABSTRACT

Numerical Simulation of the Effect of Wave Characteristics on PTO of Point Absorber Wave Energy Converter

Abigail Rolen
Department of Aerospace Engineering
Texas A&M University

Research Faculty Advisor: Mirjam Fürth
Department of Ocean Engineering
Texas A&M University

The ocean is currently an extremely large and under-developed source of renewable energy. The recent interest in the Blue Economy has led the scientific community to increase investigations in sustainable oceanic energy options, such as Point Wave Energy Converters (WEC). These devices harvest the wave energy using the excited oscillatory motion of the buoy, which is connected to a Power Take-Off system (PTO). During the last decades, the development of these devices has been boosted but they are still behind other renewable energy technologies. The Furthlab at Texas A&M University has showed that the spheroid buoy shape with a low length to diameter ratio is a good candidate shape to extract wave energy, by testing different buoy shapes and aspect ratios at a non-linear Stokes-II wave generation. This paper is the next step in our investigations and numerically investigates the effect of changing the wave characteristics, such as amplitude, frequency, and speed on the power-generating ability of the spheroid buoy system. Three-dimensional Unsteady Reynolds-Averaged Navier-Stokes (URANS) simulations of the selected buoy were performed in OpenFOAM with the integration of a dynamic mesh module to handle the heave motion of the buoy. In addition, the PTO system was compensated with a forced oscillator mechanism of spring

and damper. A comparison between the buoy's displacement and frequency responses, and power efficiency showed the optimal operating sea state to maximize energy output using the spheroid WEC. The results conclude that the best wave conditions to maximize the power extraction efficiency using a spheroid buoy with a diameter of 1 m and length of 0.5 m are wave length greater than 4 m, wave height less than 0.15 m, and wave speed between 0.07 and 0.12 m/s.

Keywords: Computational Fluid Dynamics, Ocean Energy Harvesting, Wave Characteristics, Point Wave Energy Converter, OpenFOAM

ACKNOWLEDGMENTS

Contributors

I would like to thank my faculty advisor, Dr. Mirjam Fürth[4], for her guidance and support throughout the course of this research.

This project was a team effort between Abigail Rolen[1], Ahmed A. Hamada[2], and William McCullough[3]. This same project was presented at the Society of Marine Architects and Naval Engineers (SNAME) Offshore Symposium on February 22nd, and will be published at OnePetro.org.

Computational resources used for Numerical Simulation of the effect of wave characteristics on PTO of Point Absorber WaveEnergy Converter were provided by the Texas A&M Department of Ocean Engineering.

All other work conducted for the thesis was completed by the students independently.

Funding Sources

Undergraduate research was supported by the Undergraduate Summer Research Grant program at Texas A&M University.

Department of Aerospace Engineering[1],
Department of Ocean Engineering[2],
Department of Ocean Engineering[3],
Department of Ocean Engineering[4],
Texas A&M University

NOMENCLATURE

D	Diameter of the Buoy
L	Length of the Buoy
M_b	Mass of the Buoy
PTO	Power Take-Off
K_{pto}	Spring Stiffness of PTO
C_{pto}	Damping Coefficient of PTO
PWEC	Point Wave Energy Converter
U_i	Mean flow velocity vector
u_i	Fluctuation flow velocity vector
I_t	Turbulence intensity
$\overline{p}$	Mean kinematic pressure
k_t	Turbulence kinematic energy
ν	Kinematic viscosity
ν_t	Eddy viscosity
$-\overline{u_i u_j}$	Kinematic Reynolds-stress tensor
ϵ_t	Turbulence dissipation rate
l_t	Characteristic length scale
ω_t	Specific turbulence dissipation rate
F_z	Applied force on the buoy in the z-direction
m^*	Mass ratio
f_n	Natural frequency
ζ	Damping ratio
M_A	Added mass

M_d	Displaced Mass
K_r	Restoring force
A_w	Wetted surface of the buoy
P_c	Average wave energy conversion power
P_w	Incident wave power
η_P	Extracted power efficiency
η_H	Height efficiency
$\overline{H_b}$	Average height of the buoy motion
H_w	Incident wave height
N_{cell}	Number of cells in the mesh
z_{fp}	Flotation point
z_{cg}	Center of gravity point

1. INTRODUCTION

Wave Energy Converters (WECs) are an emerging technology that aims to harvest renewable energy from the motion of ocean waves. With the increasing concerns about global warming, many countries are moving towards increasing their renewable energy usage, to decrease their carbon footprint. In particular, the U.S. and Canada are working to develop next-generation maritime or "blue" renewable energy devices, such as WEC, in response to the demand for "powering the Blue Economy" (NOAA, 2021; Pacific Northwest National Laboratory, 2022; Government of Canada, 2021). The Blue Economy is defined according to The World Bank (2017) as "the sustainable use of ocean resources for economic growth, improved livelihoods, and jobs while preserving the health of ocean ecosystems." This has caused the scientific community focus on optimizing the performance of renewable energy sources, such as WEC. WEC works by harnessing the mechanical energy from the motion of ocean waves and transforming it into electricity. The focus of this paper is a buoy constrained to a single degree of freedom, called a Point Wave Energy Converter (PWEC). A PWEC harvests wave energy from the heave motion of the buoy (Wen et al., 2018). The buoy is connected to the Power Take-Off system (PTO), which acts as a damping system during the conversion of the mechanical motion of the buoy into electricity (López et al., 2017). By constraining the buoy to only move in heave direction, the impact of changes in wave properties can be directly observed.

Optimizing the buoy shape increases the PWEC's response motion, which increase the extracted power (Aderinto and Li, 2018). However, the literature do not provide a single universally optimized buoy shape; it changed from study to study with the wave characteristics, as shown in Figure 1.1b. Shadman et al. (2018) used the Design Of Experiment (DOE) method to optimize the buoy geometry of a PWEC near the coast of Rio de Janeiro, where the predominant wave period ranges between 7 and 13 s with an average significant height of 1.33 m. Their study concluded that a cylindrical buoy shape with a diameter of $D = 13.5$ m and a length of $L = 3$ m was optimal.

A multi-objective optimization study by Kurniawan and Moan (2012) concluded that the elliptical shape was the best energy harvesting buoy shape when examining a uniform distribution of wave frequencies from 0.4 to 1.3 rad/s. Goggins and Finnegan (2014) found a truncated cylinder with a hemisphere attached at its base achieved the optimal heave velocity response in irregular waves over a frequency range of 0 to 0.2 Hz and an amplitude range between 0 and 2.75m. Further, a uni-symmetric shape with a bulbous body and wings, presented by McCabe et al. (2010); McCabe (2013), was the optimized buoy shape in irregular waves 40 km west of the Shetland Islands, where the frequency range is $[0 - 4]$ rad/s and the amplitude range is $[0.75 - 6.75]$ m. Pastor and Liu (2014) analysed a buoys with a hemispherical bottom and a conical bottom over frequencies ranging between 0.2626 and 2.5849 rad/s and amplitudes between 0.25 and 3.75m. They found that the cone-cylinder buoy performed slightly better than the hemispherical buoy. Khojasteh and Kamali (2016) also found that the conical buoy outperforms the spherical in wave flume experimental trials on a 1/15.9 scale, with frequencies between 0 and 0.4Hz and amplitudes of 8 and 10.2 cm. In addition, Hamada and Fürth (2021) compared different buoy shapes (cylindrical buoy, cylindrical with a hemisphere buoy, cylindrical with a 45° conical buoy, hemi-ellipsoidal buoy, and spheroid buoy) to investigate the power extraction efficiency of these shapes on the Power Take-Off (PTO). They found that a spheroid shape was effective at harvesting ocean energy, due to the large waterplane area and low length-to-diameter ratio in waves with a 0.625Hz frequency and a 0.2m wave height.

The first Variable Shape PWEC (VSPWEC) was proposed by Zou and Abdelkhalik (2020). This buoy can change its shape depending on the incident wave. This is mainly aimed at eliminating the reactive power needed in the PTO unit and sequentially increases the energy harvesting efficiency. Shabara et al. (2021) further investigated the performance of the VSPWEC using high-fidelity simulations, where an 8% increase in harvested power compared to the Fixed Shape PWEC (FSPWEC) was achieved. With the use of active shape optimization, optimal control algorithms and excitation wave estimation (Zou et al., 2021; Abdelkhalik et al., 2017), the VSPWEC can outperform FSPWECs due to their wider optimal operation ranges under different sea conditions and less complex PTO units.

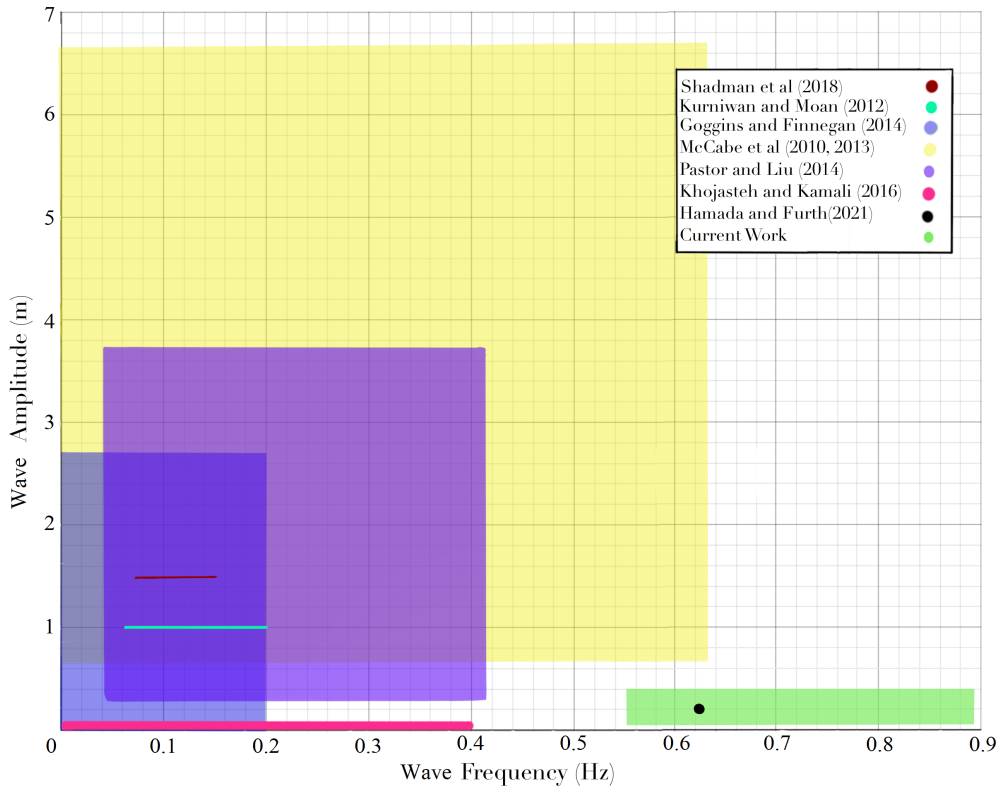

(a) Ranges of wave frequencies and wave heights tested in the aforementioned literature.

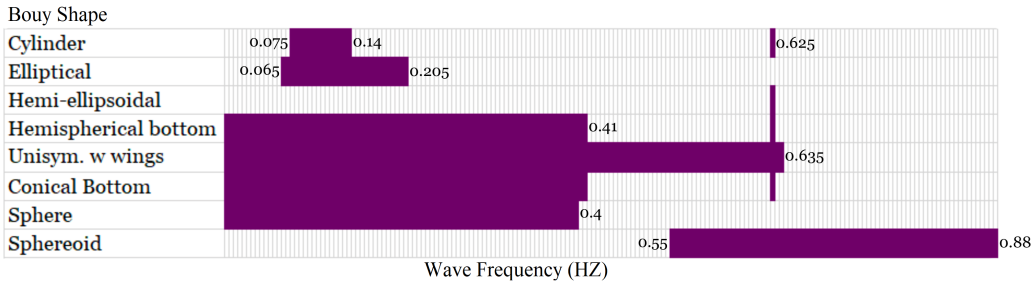

(b) Range of wave frequencies tested for different buoy shapes in the aforementioned literature.

Figure 1.1: Categorizing the literature according to the tested wave frequencies, wave heights, and buoy shapes.

It is clear that the wave characteristics greatly influence the optimal buoy shape, summarized in Figure 1.1. Therefore, it is essential to determine the range of optimal operation for each common shape of FSPWECs, starting with the spheroid buoy shape, as recommended by Hamada and Fürth (2021). The objective of this paper is to numerically determine the best operational conditions for energy harvesting using a spheroid buoy PWEC. This was achieved by studying the

amplitude and frequency responses, and the power extraction efficiency of the buoy.

2. COMPUTATIONAL MODEL

This section describes the computational model that was used to simulate the PWEC including the spheroid buoy shape and the PTO system in different sea states. In addition, the governing equations of the multi-phase flow, the equation of motion, and the equations of power extraction and efficiency were presented. The governing equations of the multi-phase flow were first used to solve the hydrostatic and hydrodynamic forces applied on the buoy due to the incoming waves. Then, the equation of motion was solved to determine the new heave position of the buoy, considering the effect of the PTO system. An iterative loop between these two sets of equations marched with time. Then, the power model was implemented on the steady-state part of the results to indicate the efficiency of the spheroid buoy in the tested waves. Next, the computational Domain of the problem was presented briefly, including the numerical solver and the used grid. Further, more details were included in our previous work (Hamada and Fürth, 2021).

2.1 Model Description

A spheroid buoy was partially submerged in a two-phase flow of water and air and was subjected to a Stokes wave (Stokes, 1880). The buoy heaves along the z-direction due to the applied excitation force, F, on the buoy surface, from the wave motion. A low aspect ratio, L/D, of 0.5 was chosen for the buoy shape because the power extraction from the waves using a spheroid buoy shape increases as the aspect ratio decreases (Hamada and Fürth, 2021). The buoy had a 1m diameter, a 0.5m length, and a mass of M_b, as shown in Figure 2.1. The centroid of the volume of

Table 2.1: Chosen wave characteristics for the simulated cases.

	Reference Case	Varied wave height			Varied wave length			Varied wave speed			
Case#	0	1	2	3	4	5	6	7	8	9	10
H_w (m)	0.2	0.05	0.1	0.4	0.2	0.2	0.2	0.2	0.2	0.2	0.2
λ_w (m)	4	4	4	4	3	5	6	4	4	4	4
$\overline{U_1}$ (m/s)	0.03	0.03	0.03	0.03	0.03	0.03	0.03	0.06	0.09	0.12	0.15

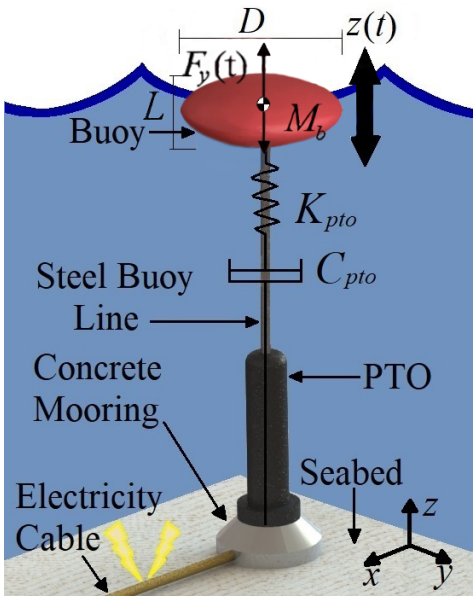

Table 1: System and fluid properties

Length to diameter ratio, L/D	0.5
Buoy diameter, D_b	1 m
Buoy mass, M_b	220 kg
Spring stiffness, K_{pto}	1.6×10^6 N/m
Damping coefficient, C_{pto}	3000 Ns/m
Mean wave velocity, $\overline{U_1}$	$[0.03 - 0.15]$ m/s
Wave height, H_w	$[0.05 - 0.8]m$
Wave length, λ_w	$[2 - 6]m$
Wave frequency, f_w	$[0.88 - 0.51]Hz$
Simulation final time, t_f	20 s
Steady-state time range, t_{ss}	$12.5 - 20$ s
Water Density, ρ_w	1000 kg/m^3
Air Density, ρ_a	1.2 kg/m^3
Water kinematic viscosity, ν_w	1×10^{-6} m^2/s
Air kinematic viscosity, ν_a	1.48×10^{-5} m^2/s

Figure 2.1: Schematic of the structure of the PWEC with a spheroid buoy shape. The buoy oscillates vertically, and the PTO is modeled with a spring and damper.

the buoy was leveled with the undisturbed free surface of the water ($z = 0$), with the positive z-direction pointing upwards. The PTO system was modeled by a spring, K_{pto}, and a damper, C_{pto}, describing the buoy motion in the z-direction as a linear spring-mass-damper freely oscillating system. The properties of the fluids; water and air, were each kept constant. These values and the Stokes wave parameters are listed in Table 2.1. The wave flow was in the positive x-direction, and the wave velocity, height, and wavelength were varied for each case considering a deep water condition, as shown in Table 2.1. Furthermore, case 0 represents the case that was performed by Hamada and Fürth (2021) and was used as a reference case. These parameters were chosen to reflect sea states between 1 and 3 on the Beaufort sea scale with no wind dependence (Beaufort, 1805).

2.2 Governing Equations

Here, the *interDyMFoam* solver, implemented in the OpenFOAM® CFD package was used. *InterDyMFoam* is an extension of *interFoam*, which calculates the flow field for two incompress-

ible fluids using a Volume of Fluid (VoF) approach. *InterDyMFoam* makes use of the optional mesh refinement- here, the mesh motion is refined close to the buoy. *InterDyMFoam* solves the Unsteady Reynolds-Averaged Navier-Stokes (URANS) equations (Ferziger et al., 2002), which are composed of the averaged continuity and momentum equations, and are expressed as:

$$\frac{\partial \overline{U_i}}{\partial x_i} = 0 \tag{Eq. 1a}$$

$$\frac{\partial \overline{U_i}}{\partial t} + \overline{U_j}\frac{\partial \overline{U_i}}{\partial x_j} + \frac{\overline{u_i u_j}}{\partial x_j} = -\frac{\partial \overline{p}}{\partial x_i} + \nu \frac{\partial^2 \overline{U_i}}{\partial x_j \partial x_j} \tag{Eq. 1b}$$

where $\overline{U_i}$ represents the mean flow velocity components in three directions; x, y, and z, u_i is the fluctuation flow velocity components, $\overline{p}$ is the mean kinematic pressure of the fluid flow, ν is the kinematic viscosity of the fluid, and $-\overline{u_i u_j}$ is the kinematic turbulent Reynolds-stress tensor. Ensuring the solenoidal velocity field is achieved by retrieving the coupling between the continuity and the momentum equations with the Poisson equation, which its averaged equation is expressed as:

$$\frac{\partial^2 \overline{p}}{\partial x_i \partial x_i} = -\frac{\partial \overline{U_i}}{\partial x_j}\frac{\partial \overline{U_j}}{\partial x_i} - \frac{\partial^2 \overline{u_i u_j}}{\partial x_i \partial x_j} \tag{Eq. 1c}$$

The $k_t - \epsilon_t$ RANS equations are used to model the turbulence in the flow field, and it is depending on the standard model (Launder and Spalding, 1983) and the rapid distortion theory compression term (El Tahry, 1983). The governing equations of the $k_t - \epsilon_t$ RANS model are expressed as:

$$\frac{\partial k_t}{\partial t} + \overline{U_i}\frac{\partial k_t}{\partial x_j} = -\overline{u_i u_j}\frac{\partial \overline{U_i}}{\partial x_j} - \epsilon + \frac{\partial}{\partial x_j}\left[\left(\nu + \frac{\nu_t}{\sigma_k}\right)\frac{\partial k_t}{\partial x_j}\right] \tag{Eq. 2a}$$

$$\frac{\partial \epsilon_t}{\partial t} + \overline{U_j}\frac{\partial \epsilon_t}{\partial x_j} = -C_{\epsilon_1}\frac{\epsilon_t}{k_t}\overline{u_i u_j}\frac{\partial \overline{U_i}}{\partial x_j} - C_{\epsilon_2}\frac{\epsilon_t^2}{k_t} + \frac{\partial}{\partial x_j}\left[\left(\nu + \frac{\nu_t}{\sigma_\epsilon}\right)\frac{\partial k_t}{\partial x_j}\right] \tag{Eq. 2b}$$

where k_t and ϵ_t are the turbulent kinetic energy and the turbulent dissipation rate, respectively. The values of the closure coefficients of the standard $k - \epsilon$ model, C_{ϵ_1}, C_{ϵ_2}, σ_k, and σ_ϵ, are 1.44, 1.92, 1, and 1.3, respectively.

Furthermore, the eddy viscosity, ν_t, and the specific turbulence dissipation rate, ω_t, are defined in terms of the turbulent kinetic energy, k_t, and the turbulence energy dissipation rate, ϵ_t, as:

$$\nu_t = C_\mu \frac{k_t^2}{\epsilon_t} \tag{Eq. 3a}$$

$$\omega_t = \frac{\epsilon_t}{C_\mu k_t} \tag{Eq. 3b}$$

where C_μ is the turbulence model constant, and equals 0.09.

2.3 Equations Of Motion

A second-order linear ordinary differential equation of time t models the mass-spring-damper system that represents the heave motion of PWEC, and is expressed as:

$$M_b \ddot{z}(t) + C_{pto} \dot{z}(t) + K_{pto} z(t) = F_z(t) - M_b g \tag{Eq. 1}$$

Where M_b is the mass of the buoy, C_{pto} and K_{pto} are the mechanical damping coefficient and is the elastic stiffness of the PTO. The values of C_{pto} and K_{pto} were kept constant during the simulation, and they were not the optimized values, because the aim of this research was to examine the effect of changing the wave characteristics on the power efficiency of spheroid PWEC. In addition, $F_z(t)$ represents the total hydrodynamic and hydrostatic forces applied on the buoy in the z-direction as a function of time.

A resonance with a natural frequency, f_n, is obtained when an equilibrium between the inertial force, $M_b \ddot{z}(t)$, and the restoring forces, $F_z(t) - M_b g$, happens. Thus, the non-dimensional

parameters, the mass ratio, m^*, the natural frequency, f_n, and damping ratio, ζ, are expressed as:

$$m^* = \frac{M_b}{M_d} \quad \text{(Eq. 2a)}$$

$$f_n = \frac{1}{2\pi}\sqrt{\frac{K_{pto} + K_r}{M_b + M_a}} \quad \text{(Eq. 2b)}$$

$$\zeta = \frac{C_{pto}}{2\sqrt{(K_{pto} + K_r)\,(M_b + M_a)}} \quad \text{(Eq. 2c)}$$

where M_d is the displaced mass, and M_a is the added mass (Sarpkaya, 2004). Further, K_r is the restoring spring and is simplified to be $\rho_{water} g A_w$, where A_w is the waterplane area of the buoy (Zhang et al., 2020).

2.4 Power and Efficiency Model

The performance of the tested spheroid PWEC in harvesting the energy from the incoming waves was measured using two indicators: the extracted power efficiency, η_P =, and the height efficiency, η_H, (Budar and Falnes, 1975). The first one was calculated as the ratio of the average wave energy conversion power, P_c, to the incident wave power, P_w, for a deep-water condition. While the second one was defined as the ratio of the average height of the buoy motion, $\overline{H_b}$, to the incident wave height, H_w.

$$P_c = \frac{C_{pto}}{nT}\int_t^{t+nT} V^2 dt \quad \text{(Eq. 1a)}$$

$$P_w = \frac{\rho_{water} g H_w^2 \omega_w D}{16 n_w} \quad \text{(Eq. 1b)}$$

$$\eta_P = \frac{P_c}{P_w} \quad \text{(Eq. 1c)}$$

$$\eta_H = \frac{\overline{H_b}}{H_w} \quad \text{(Eq. 1d)}$$

where H_w is the incident wave height, T is the wave period, ω_w is the wave frequency in rad/sec ($\omega = 2\pi f_w$ where f_w is the wave frequency in Hertz), n_w is the wave-number, n is the number of the buoy motion period, and V is the buoy velocity.

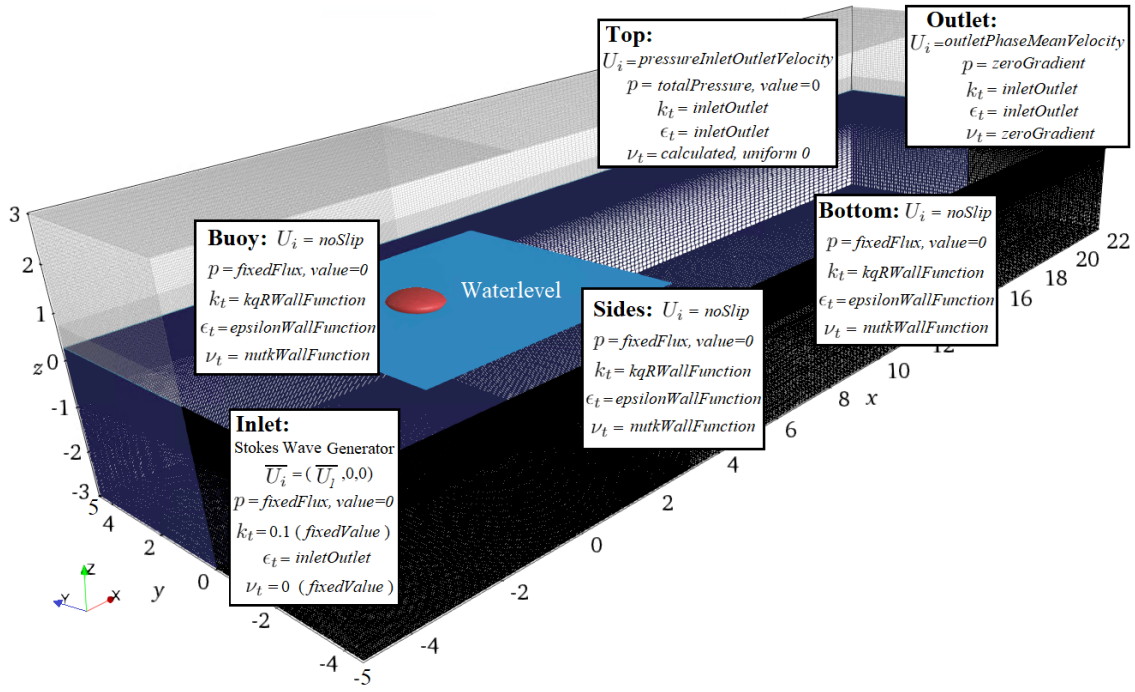

Figure 2.2: The computational domain, showing the dimension of the domain in terms of the buoy's diameter. The boundary and initial conditions are shown. The grid is clustered in the vicinity of the buoy to capture the turbulence.

2.5 Computational Domain

The *interDymFOAM* simulates the multi-phase flow using the PIMPLE algorithm, which combines the PISO (Pressure Implicit with Splitting of Operators) and SIMPLE (SemiImplicit Method for pressure-Linked Equations) algorithms Jasak (1996). The buoy is placed at $(x_b,\ y_b,\ z_b) = (5,\ 0,\ 0)$ in a rectangle computation domain of size $27m \times 10m \times 6m$ in x, y, z, respectively. The inlet wave travels along the x-axis with a given mean velocity,. Furthermore, the wave is dampened $12m$ after the buoy to ensure a smooth exit and negligible reflection. The boundary and initial conditions are shown in Figure 2.2. A three-dimensional grid was implemented to discretize the domain, with the mesh being finer close to the buoy to improve the accuracy at which the turbulence is captured. The mesh independent analysis, performed by Hamada and Fürth (2021), resulted in the selection of an 11 million cell mesh.

3. RESULTS AND DISCUSSION

The dependence of the hydrodynamic responses (amplitude and frequency ratios), and the power extraction from a single spheroid buoy on the wave characteristics (wave height, wave length, and wave speed) was investigated. Further, the change in the wave characteristics causes variation in the strength of the applied forces on the submerged part of the buoy. The simulation of each case lasts for 20 seconds to ensure the steady-state solution. Thus, the results were post-processed on the last 7.5 seconds.

3.1 Wave Height Efficiency

The steady-state displacement history, z_{cg}/D, of a single spheroid buoy for various wave heights, is shown in Figure 3.1 left. It can be seen that the amplitude, A_b, increases when the wave height, H_w, gets larger, as expected. However, the rate of increase of A_b is less than the rate of enlarging the H_w. This is reflected in the decrease of height efficiency of the buoy with the increase of H_w, as shown in the left axes of Figure 3.2. Moreover, the results of the frequency ratio, f_b/f_w, during changing H_w shows that the resonance phenomenon occurs in wave heights of 0.05, 0.1, and 0.2 as the frequency ratio is very close to 1. For larger wave height w.r.t. the geometry of the spheroid buoy, $H_w/D = 0.4$ and $H_w/L = 0.8$, the f_b/f_w decreases and considerably deviate from the resonance, reaching a value of 0.975, as shown in Figure 3.1 right. The efficiency of a spheroid buoy shape in energy harvesting, η_P, is relatively high when the buoy is exposed to a low H_w. Further, it decreases with the increase of H_w, as shown in the right axis of Figure 3.2. The reason is that the slope of the wave steepens with in the increase of H_w while the other wave characteristics (wave length, wave frequency, and wave speed) are fixed, which is reflected in the increase of the ratio, H_w/L and an impulse-like wave to face the spheroid buoy shape. This delays the response of the spheroid buoy which decreases A_b, pushes f_b/f_w far from 1, and results in sequentially lower η_P. In addition, the gain in η_P using the spheroid buoy shape is around double when the H_w decreased by a factor of 4 from 0.2 m.

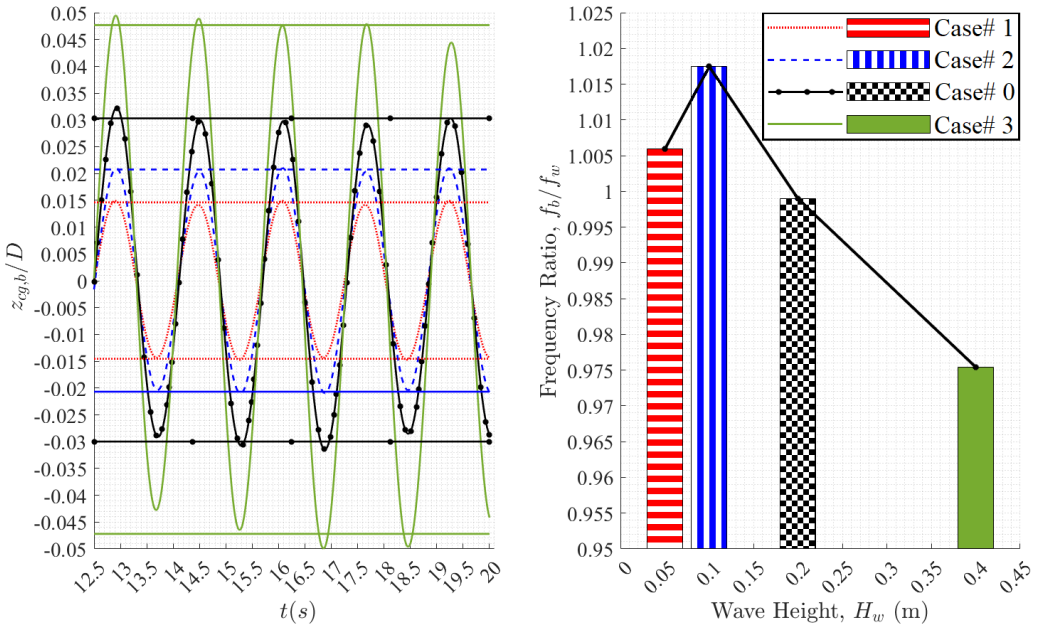

Figure 3.1: The steady-state displacement history, $z_{cg,b}/D$, and the frequency ratio, f_b/f_w, for PWEC with a spheroid buoy shape with $M_b = 200kg$, $K_{pto} = 1.6 \times 10^6 N/m$, $C_{pto} = 3000Ns/m$, and different wave heights, H_w, of the Stokes-II wave.

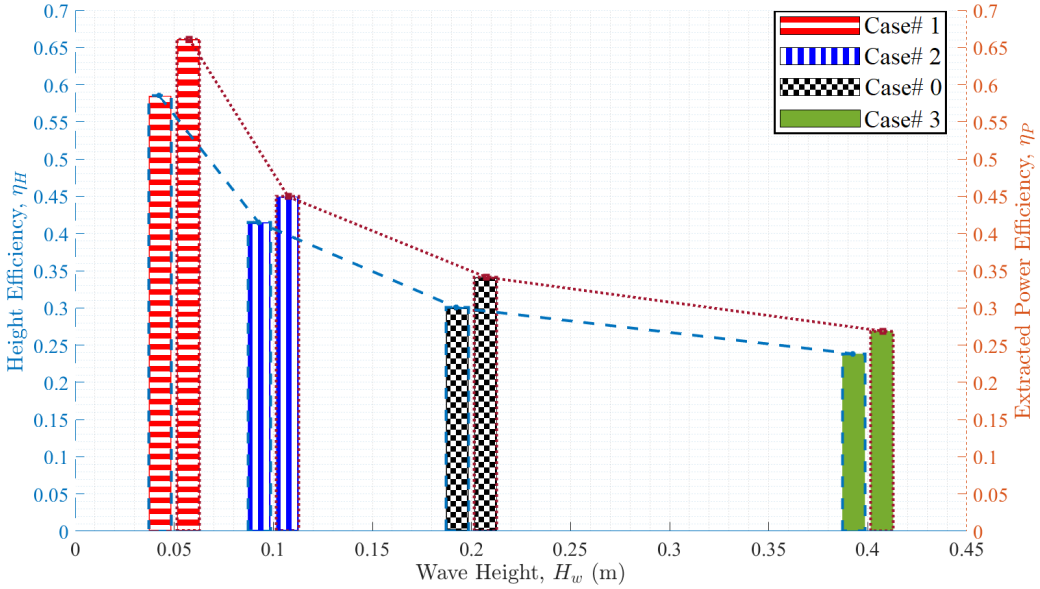

Figure 3.2: The height efficiency, η_H, and the extracted power efficiency, η_P, for PWEC with a spheroid buoy shape with $M_b = 200kg$, $K_{pto} = 1.6 \times 10^6 N/m$, $C_{pto} = 3000Ns/m$, and different wave heights, H_w, of the Stokes-II wave.

3.2 Wave Length Efficiency

The steady-state displacement history, z_{cg}/D, of the spheroid buoy increases with the increase of wave length, λ_w, as shown in Figure 3.3 left. Furthermore, the increase in λ_w, while fixing the values of wave height and wave speed at 0.2 m and 0.03 m/s respectively, enables the spheroid buoy to trace the wave slope and achieve a higher efficiency height, η_H, as shown in the left axis of Figure 3.4. In addition, the variation of the wave number slightly affects the resonance phenomenon as the values of frequency ratio, f_b/f_w, are very close to 1 in the range of wave lengths $[3-6]$, as shown in Figure 3.3 right. The increase in wave length while fixing the other wave parameters flattens the incoming wave and also increases its wave period, T. This gives the spheroid buoy, which has a relatively large waterplane area, sufficient time to respond to the incoming wave and to assimilate to the wave's slope. Thus, the extraction power efficiency, η_P, of the spheroid buoy increases with the increase of the wave lengths, as shown in the right axis of Figure 3.4. Furthermore, the increase in η_P using a spheroid buoy shape approaches an asymptote when the λ_w increases more than 4 m, reaching the value of 0.45.

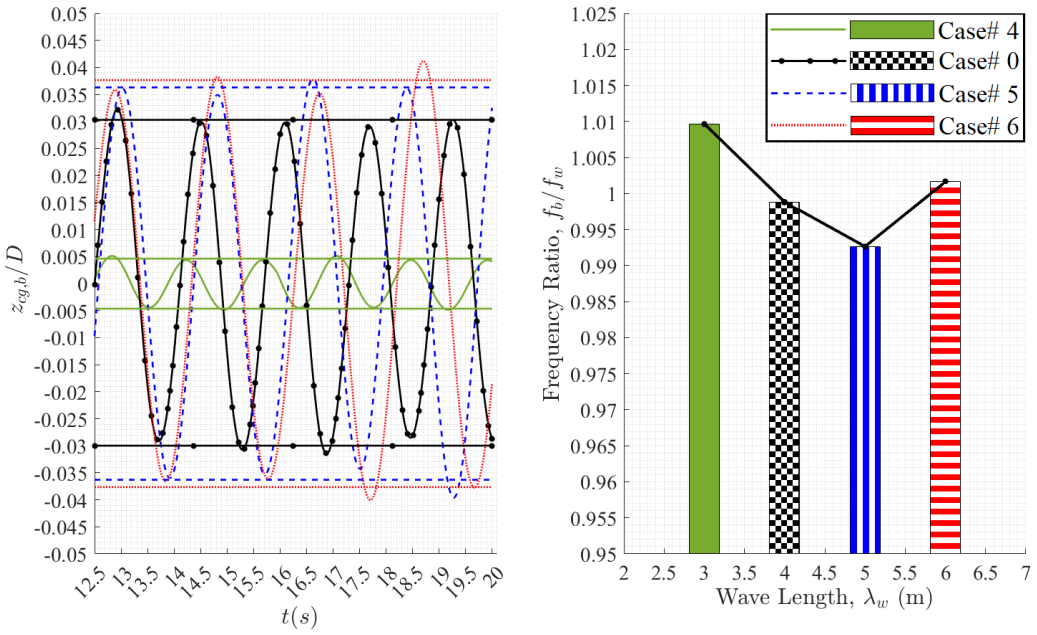

Figure 3.3: The steady-state displacement history, $z_{cg,b}/D$, and the frequency ratio, f_b/f_w, for PWEC with a spheroid buoy shape with $M_b = 200kg$, $K_{pto} = 1.6 \times 10^6 N/m$, $C_{pto} = 3000Ns/m$, and different wave lengths, λ_w, of the Stokes-II wave.

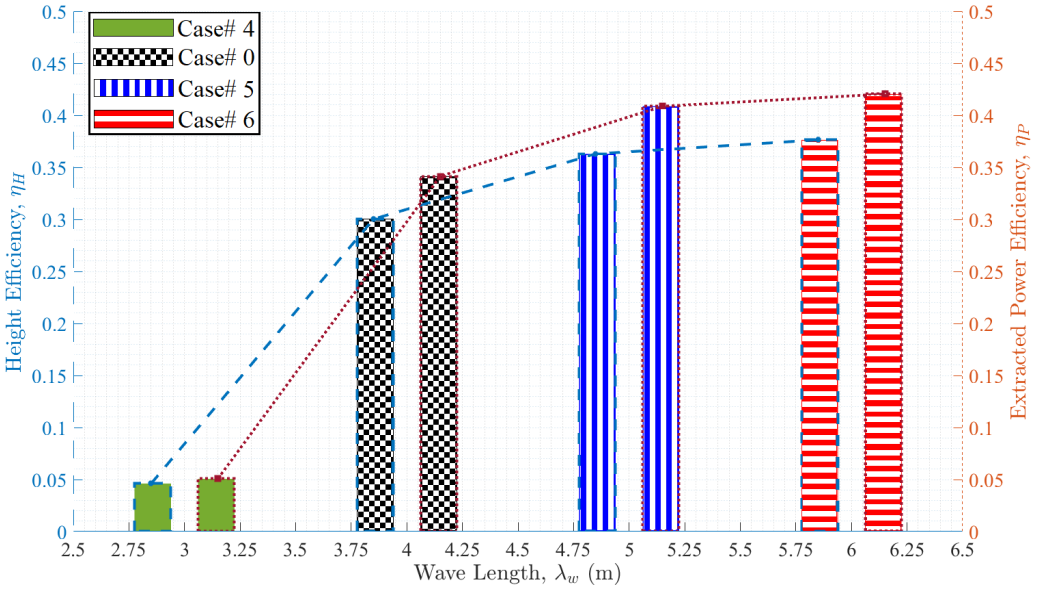

Figure 3.4: The height efficiency, η_H, and the extracted power efficiency, η_P, for PWEC with a spheroid buoy shape with $M_b = 200kg$, $K_{pto} = 1.6 \times 10^6 N/m$, $C_{pto} = 3000Ns/m$, and different wave lengths, λ_w, of the Stokes-II wave.

3.3 Wave Speed Efficiency

The steady state displacement, z_{cg}/D, of the spheroid buoy increases with an increase in wave speed, $\overline{U_1}$, as shown in Figure 3.5 left. While the wave height, H_w, and wave length, λ_w, are fixed at 0.2m and 4m, respectively, the increase in $\overline{U_1}$ lends momentum to the buoy resulting in a slight increase of η_H as shown in 3.5 left. The variation of $\overline{U_1}$ also impacts the resonance: when $\overline{U_1}$ is in the range of $[0.02 - 0.07]$ m/s, the frequency ratio remains very close to 1 as shown in Figure 3.5 right. Then, the frequency ratio continues to increase with further increases in $\overline{U_1}$, leaving the resonance/lock-in range. A spheroid buoy with a high waterplane area will respond quickly to an incoming wave due to its relatively stiff motion geometry (Budar and Falnes, 1975). This causes the buoy's extraction efficiency η_P to increase as wave speed increases. The buoy's η_P appears to reach a maximum at a $\overline{U_1}$ of around 0.12 m/s and then begin to decrease gradually, as shown in Figure 3.6. The same is true of the height efficiency, η_H.

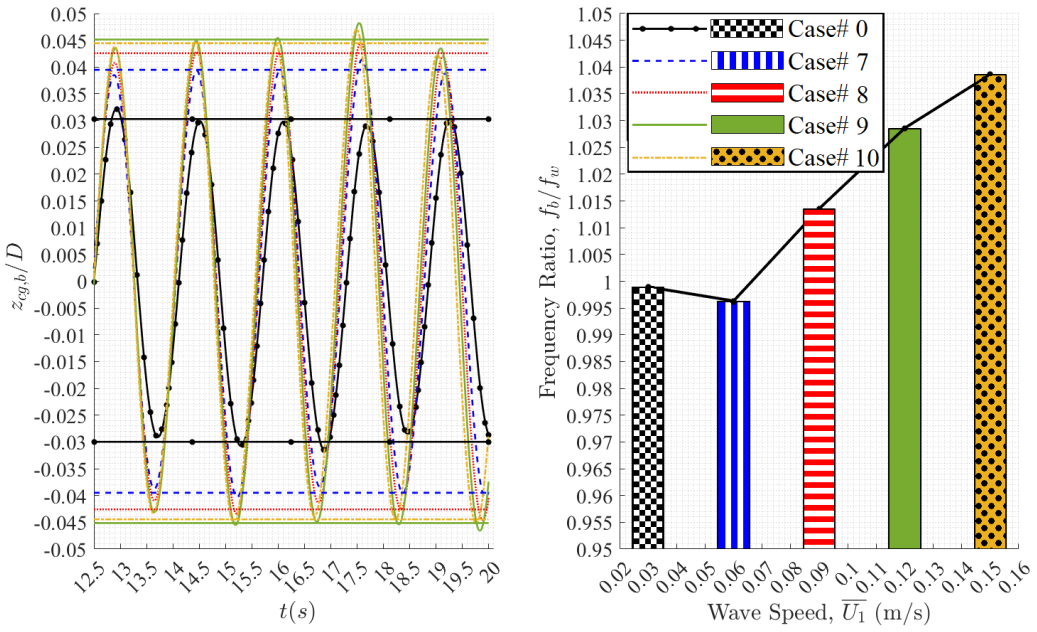

Figure 3.5: The steady-state displacement history, $z_{cg,b}/D$, and the frequency ratio, f_b/f_w, for PWEC with a spheroid buoy shape with $M_b = 200kg$, $K_{pto} = 1.6 \times 10^6 N/m$, $C_{pto} = 3000Ns/m$, and different wave speeds, $\overline{U_1}$, of the Stokes-II wave.

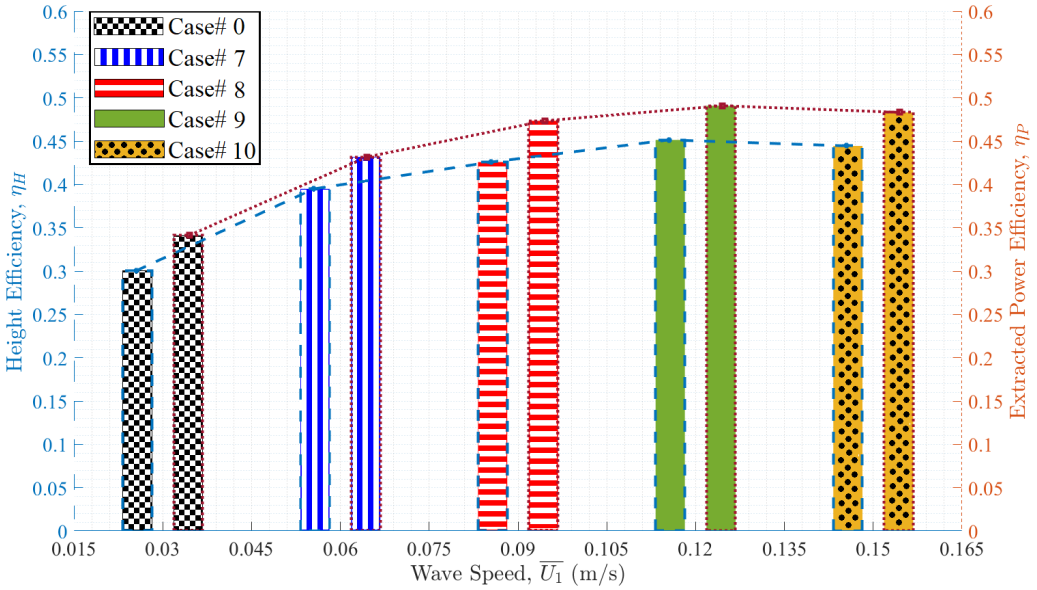

Figure 3.6: The height efficiency, η_H, and the extracted power efficiency, η_P, for PWEC with a spheroid buoy shape with $M_b = 200kg$, $K_{pto} = 1.6 \times 10^6 N/m$, $C_{pto} = 3000Ns/m$, and different wave speeds, $\overline{U_1}$, of the Stokes-II wave.

4. CONCLUSION

The purpose of this research is to numerically investigate the effect of wave characteristics on energy harvesting from a spheroid point wave energy converter. The selection of the buoy's geometry was determined based on the conclusion of the previous work by Hamada and Fürth (2021). They found that the power extraction efficiency of a spheroid buoy increases with the decrease of the geometrical ratio, L/D. The current study was executed by changing each of the following wave characteristics individually to study their direct effect: $H_w = [0.05 - 0.4]$, $\lambda_w = [3 - 6]$, and $\overline{U_1} = [0.03 - 0.15]$. A dynamic two-phase flow solver existing in OpenFOAM was used to conduct three-dimensional turbulent numerical simulations for each case. Finally, the buoy's displacement history, amplitude ratio, frequency ratio, and extracted power efficiency were studied to conclude the following:

- Despite the result that a spheroid buoy shape with low aspect ratio, L/D, resulted a higher efficiency than the other four shapes in the work of Hamada and Fürth (2021), the variation in sea state remarkably affects its power extraction efficiency.

- Increasing both the wave length, λ_w, and the wave speed, $\overline{U_1}$, while decreasing the wave height, H_w, improves the spheroid buoy's energy harvesting efficiency, which will see the most benefit when the spheroid buoy is operated in waves with $\lambda_w > 4$ m, $\overline{U_1} \in [0.07 - 0.12]$ m/s, and $H_w < 0.15$ m.

In the future, other buoy shapes such as cylindrical and hemi-ellipsoid, will be tested in a wide range of wave characteristics to recognize the optimal sea states for each buoy shape. This will provide insights when designing a Variable Shape PWEC.

REFERENCES

O. Abdelkhalik, S. Zou, R. Robinett, G. Bacelli, and D. Wilson. Estimation of excitation forces for wave energy converters control using pressure measurements. *International Journal of Control*, 90(8):1793–1805, 2017.

T. Aderinto and H. Li. Ocean wave energy converters: Status and challenges. *Energies*, 11(5): 1250, 2018.

T. W. Bank. What is the blue economy? https://www.worldbank.org/en/news/infographic/2017/06/06/blue-economy, 2017. Accessed: 2022-01-10.

S. F. Beaufort. Beaufort wind scale. https://www.spc.noaa.gov/faq/tornado/beaufort.html, 1805. Accessed: 2022-01-13.

K. Budar and J. Falnes. A resonant point absorber of ocean-wave power. *Nature*, 256(5517): 478–479, 1975.

S. El Tahry. K-epsilon equation for compressible reciprocating engine flows. *Journal of Energy*, 7:345–353, 1983.

J. H. Ferziger, M. Perić, and R. L. Street. *Computational methods for fluid dynamics*, volume 3. Springer, 2002.

J. Goggins and W. Finnegan. Shape optimisation of floating wave energy converters for a specified wave energy spectrum. *Renewable Energy*, 71:208–220, 2014.

G. Government of Canada. Blue economy strategy. https://www.dfo-mpo.gc.ca/campaign-campagne/bes-seb/index-eng.html, 2021. Accessed: 2022-01-10.

A. A. Hamada and M. Fürth. Numerical simulation of the effect of buoy geometries on pto of wave energy converters. In *SNAME Maritime Convention*. OnePetro, 2021.

H. Jasak. *Error analysis and estimation for the finite volume method with applications to fluid flows.* PhD thesis, Imperial College London (University of London), 1996.

D. Khojasteh and R. Kamali. Evaluation of wave energy absorption by heaving point absorbers at various hot spots in iran seas. *Energy*, 109:629–640, 2016.

A. Kurniawan and T. Moan. Optimal geometries for wave absorbers oscillating about a fixed axis. *IEEE Journal of Oceanic Engineering*, 38(1):117–130, 2012.

B. E. Launder and D. B. Spalding. The numerical computation of turbulent flows. In *Numerical prediction of flow, heat transfer, turbulence and combustion*, pages 96–116. Elsevier, 1983.

M. López, F. Taveira-Pinto, and P. Rosa-Santos. Influence of the power take-off characteristics on the performance of ceco wave energy converter. *Energy*, 120:686–697, 2017.

A. McCabe. Constrained optimization of the shape of a wave energy collector by genetic algorithm. *Renewable energy*, 51:274–284, 2013.

A. McCabe, G. Aggidis, and M. Widden. Optimizing the shape of a surge-and-pitch wave energy collector using a genetic algorithm. *Renewable Energy*, 35(12):2767–2775, 2010.

NOAA. Noaa finalizes strategy to enhance growth of american blue economy. https://www.noaa.gov/stories/noaa-finalizes-strategy-to-enhance-growth-of-american-blue-economy, 2021. Accessed: 2022-01-14.

P. Pacific Northwest National Laboratory. The blue economy advancing the power of the ocean. https://www.pnnl.gov/blue-economy, 2022. Accessed: 2022-01-10.

J. Pastor and Y. Liu. Power absorption modeling and optimization of a point absorbing wave energy converter using numerical method. *Journal of Energy Resources Technology*, 136(2), 2014.

T. Sarpkaya. A critical review of the intrinsic nature of vortex-induced vibrations. *Journal of fluids and structures*, 19(4):389–447, 2004.

M. A. Shabara, S. Zou, and O. Abdelkhalik. Numerical investigation of a variable-shape buoy wave energy converter. In *International Conference on Offshore Mechanics and Arctic Engineering*, volume 85192, page V009T09A013. American Society of Mechanical Engineers, 2021.

M. Shadman, S. F. Estefen, C. A. Rodriguez, and I. C. Nogueira. A geometrical optimization method applied to a heaving point absorber wave energy converter. *Renewable energy*, 115: 533–546, 2018.

G. G. Stokes. On the theory of oscillatory waves. *Transactions of the Cambridge philosophical society*, 1880.

Y. Wen, W. Wang, H. Liu, L. Mao, H. Mi, W. Wang, and G. Zhang. A shape optimization method of a specified point absorber wave energy converter for the south china sea. *Energies*, 11(10): 2645, 2018.

H. Zhang, B. Zhou, C. Vogel, R. Willden, J. Zang, and L. Zhang. Hydrodynamic performance of a floating breakwater as an oscillating-buoy type wave energy converter. *Applied Energy*, 257: 113996, 2020.

S. Zou and O. Abdelkhalik. Modeling of a variable-geometry wave energy converter. *IEEE Journal of Oceanic Engineering*, 2020.

S. Zou, O. Abdelkhalik, and M. Shabara. High-fidelity numerical study of in-line excitation force estimation for wave energy converters. In *The 14th European Wave and Tidal Energy Conference*, 2021.